The Astrophysical Journal, 962:147 (13pp), 2024 February 20 https://doi.org/10.3847/1538-4357/ad187d

Properties of an Interplanetary Shock Observed at 0.07 and 0.7 au by Parker Solar Probe and Solar Orbiter

Domenico Trotta[1], Andrea Larosa[2], Georgios Nicolaou[3], Timothy S. Horbury[1], Lorenzo Matteini[1], Heli Hietala[2], Xochitl Blanco-Cano[4], Luca Franci[1], C. H. K Chen[2], Lingling Zhao[5,6], Gary P. Zank[5,6], Christina M. S. Cohen[7], Stuart D. Bale[8,9], Ronan Laker[1], Nais Fargette[1], Francesco Valentini[10], Yuri Khotyaintsev[11], Rungployphan Kieokaew[12], Nour Raouafi[13], Emma Davies[14], Rami Vainio[15], Nina Dresing[15], Emilia Kilpua[16], Tomas Karlsson[17], Christopher J. Owen[3], and Robert F. Wimmer-Schweingruber[18]
[1] The Blackett Laboratory, Department of Physics, Imperial College London, London, SW7 2AZ, UK; d.trotta@imperial.ac.uk
[2] Department of Physics and Astronomy, Queen Mary University of London, London, E1 4NS, UK
[3] Department of Space and Climate Physics, Mullard Space Science Laboratory, University College London, Dorking, Surrey, RH5 6NT, UK
[4] Departamento de Ciencias Espaciales, Instituto de Geofísica, Universidad Nacional Autónoma de México, Ciudad Universitaria, Ciudad de México, Mexico
[5] Center for Space Plasma and Aeronomic Research (CSPAR), University of Alabama in Huntsville, Huntsville, AL 35805, USA
[6] Department of Space Science, University of Alabama in Huntsville, Huntsville, AL 35899, USA
[7] California Institute of Technology, Pasadena, CA 91125, USA
[8] Physics Department, University of California, Berkeley, CA 94720-7300, USA
[9] Space Sciences Laboratory, University of California, Berkeley, CA 94720-7450, USA
[10] Dipartimento di Fisica, University of Calabria, Rende I-87036, Italy
[11] Swedish Institute of Space Physics, Uppsala, Sweden
[12] Institut de Recherche en Astrophysique et Planétologie, CNRS, UPS, CNES, 9 Ave. du Colonel Roche F-31028 Toulouse, France
[13] Johns Hopkins Applied Physics Laboratory, Laurel, MD 20723, USA
[14] Austrian Space Weather Office, GeoSphere Austria, A-8020 Graz, Austria
[15] Department of Physics and Astronomy, University of Turku, FI-20014 Turku, Finland
[16] Department of Physics, University of Helsinki, Helsinki, Finland
[17] KTH Royal Institute of Technology, Stockholm, Sweden
[18] Institute of Experimental and Applied Physics, Kiel University, D-24118 Kiel, Germany
Received 2023 October 5; revised 2023 December 19; accepted 2023 December 22; published 2024 February 15

Abstract

The Parker Solar Probe (PSP) and Solar Orbiter (SolO) missions opened a new observational window in the inner heliosphere, which is finally accessible to direct measurements. On 2022 September 5, a coronal mass ejection (CME)-driven interplanetary (IP) shock was observed as close as 0.07 au by PSP. The CME then reached SolO, which was radially well-aligned at 0.7 au, thus providing us with the opportunity to study the shock properties at different heliocentric distances. We characterize the shock, investigate its typical parameters, and compare its small-scale features at both locations. Using the PSP observations, we investigate how magnetic switchbacks and ion cyclotron waves are processed upon shock crossing. We find that switchbacks preserve their V–B correlation while compressed upon the shock passage, and that the signature of ion cyclotron waves disappears downstream of the shock. By contrast, the SolO observations reveal a very structured shock transition, with a population of shock-accelerated protons of up to about 2 MeV, showing irregularities in the shock downstream, which we correlate with solar wind structures propagating across the shock. At SolO, we also report the presence of low-energy ($\sim$100 eV) electrons scattering due to upstream shocklets. This study elucidates how the local features of IP shocks and their environments can be very different as they propagate through the heliosphere.

Unified Astronomy Thesaurus concepts: Interplanetary shocks (829); Solar wind (1534); Heliosphere (711)

1. Introduction

Collisionless shock waves are present in a large number of astrophysical systems, and they are pivotal for efficient energy conversion and particle acceleration in our Universe (e.g., Richardson 2011; Bykov et al. 2019). Generally speaking, shocks convert directed flow energy (upstream) into heat and magnetic energy (downstream), and in the collisionless case, a fraction of the available energy is channeled into the production of energetic particles.

Shocks in the heliosphere are unique, being directly accessible by spacecraft exploration, thus providing the missing link to the remote observations of astrophysical systems (Richardson 2011). Most of our knowledge about the in situ properties of collisionless shocks comes from the Earth's bow shock (Eastwood et al. 2015), due to its convenient location (Dungey 1979; Wilkinson 2003). Shocks besides the Earth's bow shock are not as well observed and understood. Interplanetary (IP) shocks are generated as a consequence of solar activity phenomena, such as coronal mass ejections (CMEs; e.g., Gosling et al. 1974; Webb & Howard 2012; Kilpua et al. 2017) and stream interaction regions (SIRs; e.g., Dessler & Fejer 1963; Richardson 2018; Pérez-Alanis et al. 2023). As elucidated in decades of observations, IP shocks are generally weaker and show larger radii of curvature with respect to the Earth's bow shock, thus allowing the study of collisionless shocks in highly different regimes (see Kilpua et al. 2015).

IP shocks play an important role for the overall heliosphere energetics, due to their ability to accelerate particles to high

energies and influence the plasma environment in their surroundings (see Reames 1999, for a review). Interestingly, the nature of such an interaction between IP shocks and the complex, turbulent solar wind is still largely unknown (Guo et al. 2021). Several studies have addressed the interaction of IP shocks with various kinds of pre-existing structures (e.g., Nakanotani et al. 2021; Zank et al. 2021; Pitna et al. 2023) as well as fully developed turbulence (Pitňa 2017; Zank et al. 2021; Zhao et al. 2021). From this point of view, important insights have also been provided by means of numerical modeling, looking at large-scale, magnetohydrodynamics (MHD) behavior (Giacalone 2005; Wijsen et al. 2023), as well as the small-scale, kinetic behavior of the shock system (Trotta et al. 2021; Nakanotani et al. 2022). A complex picture is emerging, where shocks strongly influence the plasma environment in which they propagate, while they are strongly influenced by the self-induced and pre-existing irregularities they encounter (Kajdič et al. 2021; Turc et al. 2023). Such a picture is corroborated by theoretical studies of the shock–turbulence interaction (Zank et al. 2015, 2021), and it has been tested in the framework of Earth's bow shock (Sundberg et al. 2016; Schwartz et al. 2022).

IP shocks have also been shown to evolve and change their behavior at different heliocentric distances, as elucidated by early Helios observations in the inner heliosphere (Lai et al. 2012) and by Ulysses observations between 1 and 5 au (e.g., Burton et al. 1992; Zhao et al. 2018), making the study of IP shocks in different heliospheric environments particularly interesting. From this point of view, the Parker Solar Probe (PSP; Fox et al. 2016) and Solar Orbiter (SolO; Müller et al. 2020) missions are opening a novel observational window for IP shocks at previously unexplored, small heliocentric distances. Therefore, the early stages of shock evolution can be probed, and it is possible to investigate how collisionless shocks influence the plasma environment close to the Sun. Examples of studies where such new observational capabilities have been exploited are the new multi-spacecraft observations of Solar Energetic Particle events (Dresing et al. 2023), the CMEs exhibiting ion dropouts as observed by PSP (Giacalone et al. 2021), and the recent crossing of a CME leg by PSP at a distance of 14 Solar Radii (McComas et al. 2023). A thorough investigation of the event reported in this paper, addressing the interaction between the CME and the heliospheric current sheet with a combination of remote and in situ PSP observations, is reported in Romeo et al. (2023). Long et al. (2023) investigated the presence and eruption of a magnetic flux rope for this event, also combining remote-sensing and direct observations. SolO in situ measurements were also recently used together with Wind (at 1 au) to understand how shocks interact with and influence their environments at different heliocentric distances (e.g., Zhao et al. 2021). Recently, joint PSP–SolO observations elucidated the evolution of a slow plasma parcel from the solar corona to the inner heliosphere (Adhikari et al. 2022). SolO also provided important insights into the production and dynamics of energetic particles at IP shocks (Yang et al. 2023), exploiting the unprecedented quality of energetic particle measurements of the Energetic Particle Detector (EPD; Rodríguez-Pacheco et al. 2020) suite.

In this work, we study a CME-driven IP shock seen by PSP at very small heliocentric distances (0.07 au). We characterize the shock parameters and environment, and study how the shock interacts with upstream switchbacks (SBs), i.e., Alfvénic

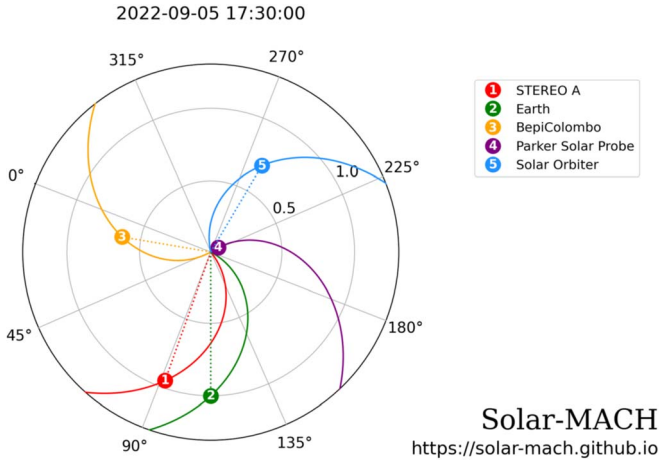

Figure 1. Spacecraft configuration at 17:30 UT of 2022 September 5 (immediately after the IP shock crossed PSP). In this plot (generated using the Solar MAgnetic Connection HAUS tool, Solar-MACH; Gieseler et al. 2023), the Sun is at the center, the Earth is represented by the green circle, and the dashed (solid) lines indicate the spacecraft radial (along a Parker spiral with a nominal speed of 400 km s^{-1}) connection.

fluctuations typical of the inner heliosphere. SB observations have been pivotal for the PSP mission, and they are emerging as a fundamental building block of the solar wind at low heliocentric distances (e.g., Bale et al. 2019; Kasper et al. 2019; Dudok de Wit et al. 2020; Bale et al. 2023; Raouafi et al. 2023), making the study of their interaction with collisionless shock waves novel and of particular interest. The CME was later observed by SolO, at a heliocentric distance of 0.7 au. SolO was radially well-aligned with PSP, thus providing us with the opportunity to study the associated shock at larger heliocentric distances and therefore later evolution time (see Figure 1). The shock at SolO is characterized by a much more structured transition, and it is stronger with respect to the PSP crossing.

The paper is organized as follows: in Section 2, we describe the data sets used and the basic parameter estimation techniques. In Section 3, we present and discuss the results, and the conclusions are reported in Section 4.

2. Data

This study focuses on the analysis of in situ magnetic field and plasma data for PSP and SolO. At PSP, we use magnetic field data from the FIELDS instrument (Bale et al. 2016), while proton density, bulk flow velocity, and temperature are obtained using the Solar Probe ANalyzer-Ions (SPAN-I; Livi et al. 2022), which is part of the Solar Wind Electrons Alphas and Protons (SWEAP) investigation suite (Kasper et al. 2016). The electron density was also estimated using the quasi-thermal noise technique (Moncuquet et al. 2020).

This work uses the entire in situ SolO instrument suite. The magnetic field is measured by the flux-gate magnetometer (MAG; Horbury et al. 2020). Ion bulk flow speed, plasma density, and temperature and electron distribution functions are obtained from the Solar Wind Analyser suite (SWA; Owen et al. 2020). The plasma density was also estimated using the SolO Radio and Plasma Waves instrument (RPW; Maksimovic et al. 2020). The SolO Energetic Particle Detector (EPD; Rodríguez-Pacheco et al. 2020) is used to investigate the properties of energetic particles at SolO. Throughout the shock event studied here, we find a discrepancy between the density estimated from the moments of the distribution function

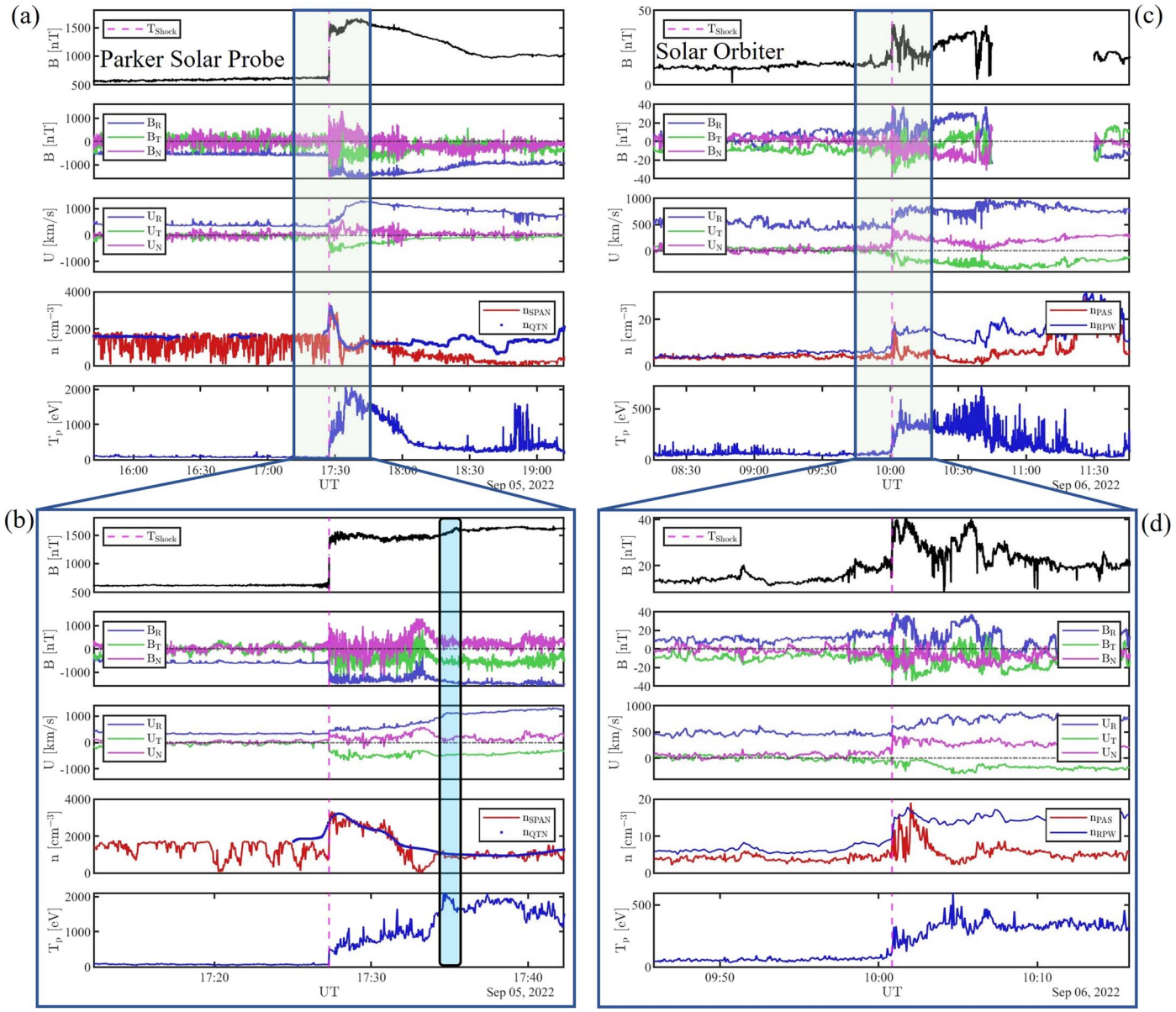

Figure 2. Magnetic field magnitude, its components in the RTN system, ion bulk flow velocity, density, and temperature as measured by PSP (left) and later on by SolO (right). The plots show an overview of the event (a, c) with a zoom-in around the shock transition at both spacecraft (b, d). The dashed magenta line marks the shock transition, and the blue shaded area in panel (b) indicates the approximate end of the CME sheath as observed by PSP.

measured by the Proton and Alpha Sensor (PAS) of the SolO SWA suite and the density estimated from the spacecraft potential using RPW (Khotyaintsev et al. 2021; see Figure 2). After analyzing the density computed as a moment of the electron distribution function (see Nicolaou et al. 2021), we decided to use the density estimated via RPW for our analysis.

3. Results

3.1. Event Overview

On 2022 September 5, a CME erupted from the Sun and into interplanetary space. The CME was not Earth directed, as the eruption happened on the far side of the Sun. An overview of the orbital configuration is shown in Figure 1.

A fast-forward shock, driven by the CME, was detected by PSP as close as 0.07 au ($\sim$15 $R_\odot$) at 17:27:19 UT, making this observation the closest to the Sun to date. An overview of the in situ magnetic field and plasma quantities is shown on the left-hand side of Figure 2. A sharp transition in magnetic field, with a jump from about 600 to about 1600 nT, occurs at the shock. The velocity profile across the shock transition shows two interesting features, namely a large flow speed deflection in the transverse direction V_T, and a steady rise in V_R further downstream, up to about 17:35. We have marked this time as the end of the downstream (sheath) region of the event, i.e., the point where the leading edge of the CME flux rope likely starts (see also Romeo et al. 2023). However, we note that the boundary between the sheath and CME flux rope is not clear for this event. The properties of the CME sheath at such low heliocentric distances (and therefore early evolutionary stages) are very interesting and will be the object of future work, comparing them with substructures and properties of CMEs at larger heliocentric distances (Kilpua et al. 2017).

We carried out a comprehensive characterization of the shock parameters locally observed by PSP. Given the density drops visible in the upstream region in Figure 2(b), due to the core of the ion distribution function not being well inside the SPAN-i field of view (Livi et al. 2022), we estimated the density using the spacecraft quasi-thermal noise (QTN) for our shock analysis. Using a systematic collection of averaging windows spanning a few seconds to three minutes (with the technique described in Trotta et al. 2022a) upstream/downstream of the shock, we used the Mixed Mode 3 method (MX3; Paschmann & Schwartz 2000) to estimate the average shock normal $\langle n \rangle = [0.5, -0.8, 0.2]$, though similar values are obtained with the other MX methods as well as magnetic coplanarity. Propagation direction deviating clearly from the radial direction is compatible with the picture in which PSP is crossing a flank of the CME event. Our estimation of $\theta_{\rm Bn}$, i.e., the angle between the shock normal and the upstream magnetic field, a crucial parameter influencing shock behavior, reveals that we are in the presence of an oblique ($\theta_{\rm Bn} \sim 53°$), supercritical shock with moderate Alfvénic and fast magnetosonic Mach numbers ($M_A \simeq 3.9$, $M_{\rm fms} \simeq 3.8$, respectively) with respect to other IP shocks observed at or near 1 au (Kilpua et al. 2015). Furthermore, we find that the shock propagates at the very high speed of about 1500 km s^{-1} in the spacecraft frame and along the estimated shock normal. At PSP, upstream of the shock, the magnetic field is mostly radial and interspersed with one-sided Alfvénic fluctuations (Gosling et al. 2009) of the magnetic field and ion bulk velocity, known as magnetic switchbacks, with moderate-amplitude angular deflections in the magnetic field, as expected for very low heliocentric distances (e.g., Jagarlamudi et al. 2023). SBs are a crucial feature of the solar wind in the inner heliosphere, as extensively shown in previous literature (Dudok de Wit et al. 2020; Krasnoselskikh et al. 2020; Larosa et al. 2021; Liang et al. 2021; Pecora et al. 2022; Jagarlamudi et al. 2023; Liu et al. 2023; Raouafi et al. 2023). Here, we have the opportunity to study how such structures are processed by shock waves, a crucial point of this work summarized in Section 3.2.

At SolO (Figure 2 right), the shock crossing appears much more structured compared to the PSP observation. Strong transverse flow deflections are still present, with a strong increase in V_N at the shock transition. The plasma density, as measured from the SWA-PAS and RPW instruments, yields two different values. For the shock parameter estimation, we used the density as measured by the RPW, because it is in agreement with the value obtained from EAS electron moments (Figure 8). However, locally computed shock parameters do not change dramatically when using the density derived from PAS. Steep upstream enhancements of magnetic field magnitude are found ahead of the shock (09:52, 09:56 UT), compatible with very rarely observed shocklets at strong IP shocks (Wilson et al. 2009; Trotta et al. 2023a). A high degree of magnetic field structuring is also found downstream of the shock, indicating a high level of complexity for this shock crossing. At SolO, the shock parameter estimation shows values very close to the ones observed at PSP (see Table 1). However, such values are obtained using very local averaging windows for the upstream/downstream quantities (∼10 s to 1 minute). The overall behavior of the shock at SolO indicates a high level of variability. Indeed, using larger averaging windows (about 6 to 10 minutes up/downstream), we find parameters compatible with a quasi-parallel shock transition ($\theta_{\rm Bn} \sim 30°$) with high Mach numbers ($M_A \sim M_{\rm fms} \sim 7$). It is worth mentioning that, in addition to the local variability examined here, a different behavior of the two shocks at PSP and SolO is expected, due to the crossing of the event at two different points in space and time. The longitudinal separation of PSP and SolO is about 20°, and depending on the CME width, the shock will be crossed in different locations. However, such a comparison of shock parameters, summarized in Table 1, is useful when addressing the evolution of the whole event, and it may be important to support remote-sensing observations of the event as well as modeling of the CME evolution.

Table 1
In Situ Shock Parameters at PSP and SolO

	Parker Solar Probe	Solar Orbiter
Shock Time (UT)	2022 September 5, 17:27:19	2022 September 6, 10:00:51
Carrington longitude (deg)	232	251.9
Carrington latitude (deg)	−1.8	−3.6
Heliocentric dist. (au)	0.07	0.7
$\langle \hat{\rm n}_{\rm RTN} \rangle$	[0.5 −0.8 0.2]	[0.6 −0.2 0.7]
$\langle \theta_{\rm Bn} \rangle$ (deg)	53	51
$\langle r_B \rangle$	2.3	1.9
$\langle r \rangle$	1.6	2
$\langle v_{\rm sh} \rangle$ (km s^{-1})	1520	942
$\beta_{\rm up}$	0.1	0.6
$M_{\rm fms}$	3.8	3.2
$M_{\rm A}$	3.9	3.8

Notes. In the table are displayed, from top to bottom, the shock arrival time, Carrington longitude and latitude at the time of shock arrival, spacecraft heliocentric distance at the time of shock arrival, shock-normal vector in RTN coordinates, shock-normal angle $\langle \theta_{\rm Bn} \rangle$, magnetic compression ratio $\langle r_B \rangle$, gas compression ratio $\langle r \rangle$, shock speed $v_{\rm sh}$, upstream plasma beta $\beta_{\rm up}$, and the fast magnetosonic and Alfvénic Mach numbers ($M_{\rm fms}$ and $M_{\rm A}$, respectively). The shock speed $v_{\rm sh}$ is along the shock normal and computed in the spacecraft rest frame using the mass flux conservation law.

It is interesting, at this point, to characterize the environment in which the shock at PSP and SolO is propagating and how it is influenced by the shock passage. To this end, we studied the magnetic fluctuations in the ∼15 minutes before/after the shock arrival, with the relevant analyses shown in Figure 3.

The shock crossing at PSP is characterized by a sharp transition, with no signs of upstream wave foreshock, as elucidated by the trace wavelet spectrogram in Figure 3(b). This is compatible with other observations of IP shocks, in particular at such oblique geometries (e.g., Blanco-Cano et al. 2016). It is worth noting that microinstabilities of the shock front happening at ion kinetic scales, such as rippling (Trotta et al. 2023b), may still be present, albeit not well resolved by PSP. The level of magnetic fluctuations is enhanced in the downstream sheath region, lasting about 6 minutes. Such an enhancement in magnetic fluctuations is further shown in Figure 3(d), where the power spectral density in the 5 minutes upstream/downstream of the shock has been computed (green and orange lines, respectively). Here, it can be seen that the level of fluctuations increases by a factor of 4, and the downstream spectra show a flattening around the ion cyclotron frequency, a behavior compatible with the spectral behavior of IP shocks (Pitňa et al. 2021), with some observations of turbulence in the Earth's bow shock environment (e.g.,

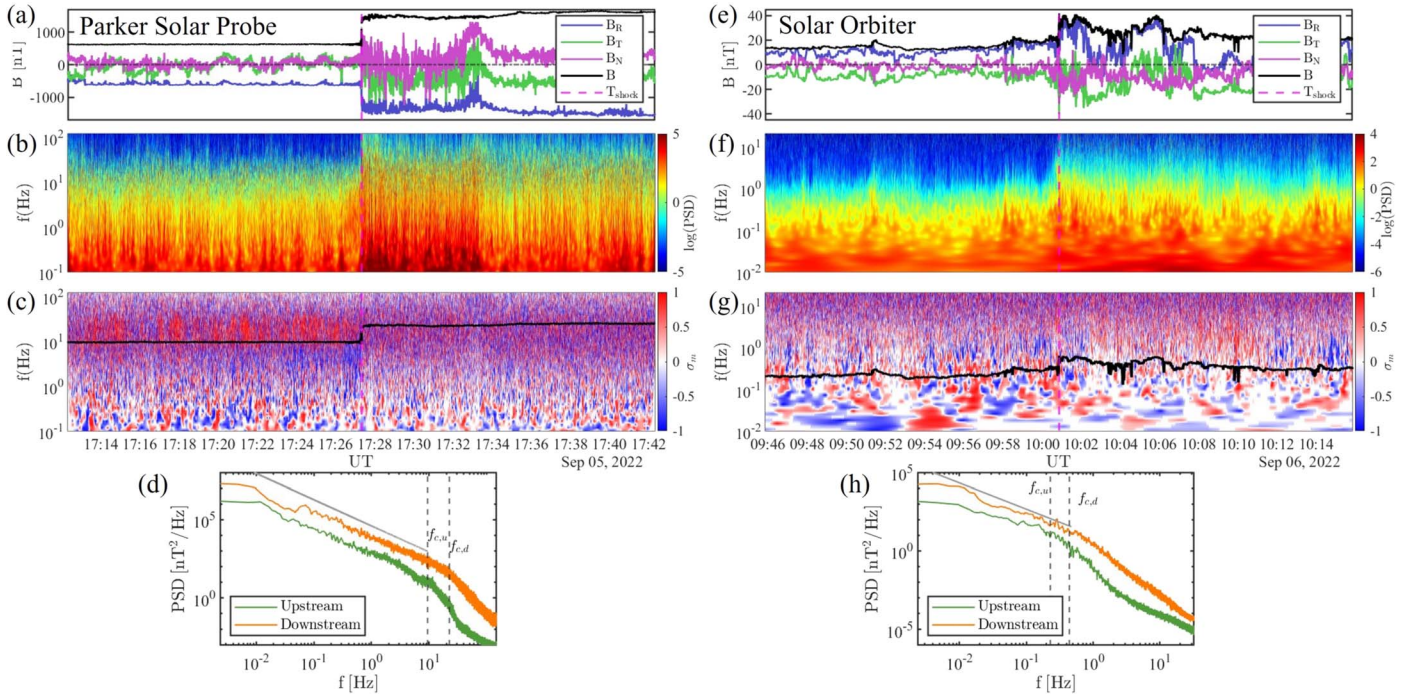

Figure 3. Magnetic fluctuations in the shock environment at PSP (left) and SolO (right). The figure shows, from top to bottom: magnetic field magnitude and its components, trace wavelet spectrogram of the magnetic field (color map), the normalized magnetic helicity σ_m spectrogram, with the proton cyclotron frequency in the interval (black line), magnetic field power spectral densities (PSDs) computed in the 10 minutes upstream (green) and downstream (orange) of the shock.

Sahraoui et al. 2020), and also with modeling of turbulence transmission across shocks (see Figure 18 in Zank et al. 2021). However, because the downstream flow speed is much larger than the upstream, and the shock changes the plasma parameters abruptly, the level of fluctuations may be overestimated. While the increase in the level of the frequency spectrum has been documented in previous literature (Zhao et al. 2021; Park et al. 2023), it remains to be understood whether IP shocks inject new turbulence or they simply modify the background plasma properties. However, preliminary analysis shows that the spectral break happens around the ion skin depth d_i, compatible with statistical work carried out by Park et al. (2023). Further studies on the matter, relevant also for understanding the behavior of turbulence at very low heliocentric distances (Zank et al. 2020), are further complicated by the geometrical constraints imposed by the single-spacecraft nature of the observations. These will be the objects of future work.

To further investigate the wave properties across the shock, we computed the normalized magnetic helicity, defined as

$$\sigma_m = \frac{2\Im(\tilde{B}_T^{\star}\tilde{B}_N)}{|\tilde{B}_R|^2 + |\tilde{B}_T|^2 + |\tilde{B}_N|^2}, \quad (1)$$

where B indicates the magnetic field components, the $\tilde{}$ represents the wavelet-transformed quantities, and $\star$ represents the complex conjugation operation (Matthaeus et al. 1982). Upstream of the shock at PSP, we observe a clear signature of consistently high σ_m at ion scales, compatible with ion cyclotron wave activity (see the red patches by the ion plasma frequency line in Figure 3(c)). Ion cyclotron waves, crucial components of the solar wind as elucidated by PSP observations (Telloni et al. 2019; Verniero et al. 2020), have been shown to be very important for energy dissipation and solar wind heating (e.g., Woodham et al. 2018; Bowen et al. 2022). In our observations, we note that the magnetic helicity signature of ion cyclotron waves found upstream of the shock is lost in the shock downstream, as discussed in Section 3.2, together with an explanation of why such a behavior is observed.

The magnetic fluctuations environment at SolO is different than that found at PSP (right-hand side of Figure 3). Here, the shock transition appears much more complex, especially due to the presence of larger-scale structures at the SolO shock with respect to the PSP one. In the wavelet spectrum of the magnetic field, enhanced power extending to small (∼1 Hz) scales is found, corresponding to the upstream shocklet activity. The downstream appears populated with strong compressive and non-compressive magnetic field fluctuations, indicative of the fact that the shock propagated through a very structured portion of the solar wind, as can be noted from the magnetic field behavior in the 10 minutes downstream of the shock (Blanco-Cano et al. 2019; Kropotina et al. 2021). The spectral behavior of turbulence in being transmitted from the shock upstream to downstream is similar to the one observed for the shock at PSP, and compatible with previous multi-spacecraft studies of turbulence processed by IP shocks (Zhao et al. 2021). It is interesting to note that, in the IP case, an inertial range is always recovered downstream of IP shocks, in contrast with some observations of Earth's magnetosheath where an inertial range is not observed downstream of Earth's bow shock (Sahraoui et al. 2020), often interpreted as the Earth's bow shock "resetting" the turbulent cascade. Finally, we note that some features of ion cyclotron wave activity are seen upstream of the SolO event, though they are much less clear than the PSP observation.

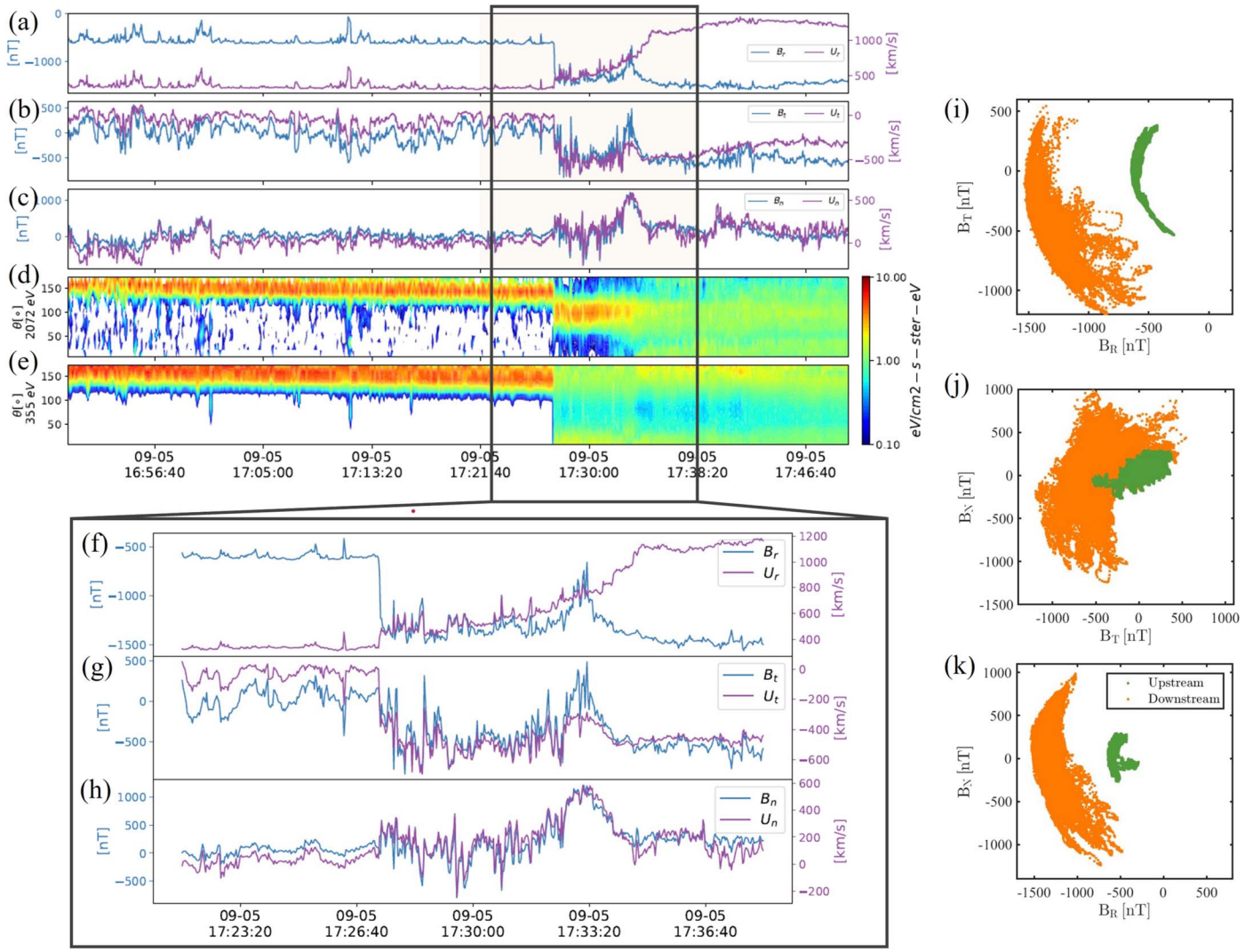

Figure 4. PSP observations of magnetic switchback transmissions across the shock. (a), (b), and (c) magnetic field (blue) and ion bulk flow velocity (plum) components. (d) and (e) pitch-angle distributions for electrons with 2072 and 355 eV energy, respectively. (f), (g), and (h) zoom-in around the shock crossing (shaded area in top panels). Scatterplots of radial and tangential (i), tangential and normal (j), and radial to normal (k) components of the magnetic field for the 4 minutes upstream of the shock crossing (green) and 4 minutes downstream of it (orange).

3.2. The Shock at Parker Solar Probe

In this section, we focus on the PSP observations of the shock interacting with pre-existing fluctuations in the inner-heliospheric solar wind and its features. Particular interest is focused on how switchbacks (SBs) are processed by the IP shock wave.

In Figure 4, we observe the high degree of correlation between the magnetic and velocity fields. The presence of moderate-amplitude SBs and their one-sided nature (Gosling et al. 2009) are especially evident in the B_R and V_R components (Figure 4(a)) upstream of the shock. In the downstream (sheath) region, the high degree of correlation is preserved, as elucidated by the zoom-ins shown in panels (f), (g), and (h) of that figure. These observations reveal that the Alfvénic nature of the SBs is preserved downstream of the shock. However, the downstream SBs present larger, shock-driven variations in the field magnitude. Small deviations from a constant B state have been already observed at SBs boundaries (Farrell et al. 2020; Krasnoselskikh et al. 2020; Larosa et al. 2021). Here, we show a different compressive effect, resulting from the propagation across the IP shock. As discussed in Section 3.1, the downstream region is characterized by stronger fluctuations driven by the shock, including small-scale, compressive fluctuations that are not Alfvénic.

From this point of view, it is interesting to note that the signature of the SBs is not completely lost upon shock passage, but rather the SBs are processed by the shock. Considering the Rankine–Hugoniot relations describing the change in plasma parameters across MHD shocks (e.g., Krehl 2015), we expect, for the SBs, a compression along the shock-normal direction and a stretch along the two shock-transverse directions. The extremely short duration of the sheath poses a strong limitation on a more quantitative study of how SB are affected by the shock. For instance, the Z parameter would be helpful in addressing such an issue (Dudok de Wit et al. 2020). Such an investigation will be carried out in future works focusing on several shocks at low heliocentric distances.

To further investigate how the shock affects the upstream SBs, we study the magnetic field excursion in the regions upstream and downstream of the shock (Figures 4(i)–(m)), as done in other studies elucidating the nature of fluctuations in the solar wind (e.g., Matteini et al. 2015). Two effects arise in

the magnetic field fluctuations after the shock crossing. First of all, due the change in background field magnitude, the arc of polarization upon which the magnetic field fluctuates become wider, as is particularly evident in the B_R–B_T scatter plot (Figure 4(i)). It is also possible to observe that downstream magnetic field fluctuations cover a larger area in the magnetic field excursion space, due to the presence of compressive fluctuations in the shock downstream. From Figures 4(i), (j), and (k), it is possible to note that the arc of polarization is displaced from the R–T plane into both the R–T and R–N planes when comparing the shock upstream to the downstream, consistent with compression along the normal and stretching along the perpendicular directions. The shock–SB interaction may have important consequences for the SBs' ability to propagate without dispersive effects, and therefore it may affect the SBs' lifetimes, because the constant B magnitude is a necessary condition for the unperturbed propagation of large-amplitude Alfvén waves (Barnes & Hollweg 1974).

The above assessment of the SBs features upstream/downstream of the shock suffers from limitations related to the single-spacecraft nature of the observations. First, it is known that the features of SBs (deflections and duration) tend to have broad distributions (e.g., Larosa et al. 2021), making it difficult to estimate the extent to which the processed, downstream SBs were comparable to their upstream, unshocked counterparts before they crossed the shock. Furthermore, how plasma is sampled by PSP throughout the observation introduces a geometrical constraint on the observations, where fluctuations are sampled differently from upstream to downstream. This latter point is further expanded in Figure 6(b) and related discussion. Another crucial caveat stems from the downstream flow speed in the spacecraft frame being much larger than that upstream, allowing more plasma to flow over the spacecraft per unit time, causing the downstream SBs to appear shorter than their upstream counterparts, an effect that appears in addition to the compression induced by the shock. Furthermore, the field increase due to the presence of the shock influences the discussion of the downstream SBs' deflection amplitude (Figure 4(i)).

For this reason, we decided to "unshock" the magnetic field and plasma time series across the PSP shock crossing. This analysis is carried out in two steps. First, using the mean upstream and downstream flow speeds, we plot the PSP measurements in units of distance from shock using the Taylor hypothesis (Taylor 1938). Then, we used the Rankine–Hugoniot jump conditions to remove the shock compression. Here, knowing the downstream quantities and the shock parameters as estimated from the spacecraft crossing (see Table 1), we derived the upstream quantities, i.e., we estimated the magnetic field and plasma conditions prior to the shock passage. Further details about this method of decompression can be found in the Appendix. The resulting, decompressed time series is shown in Figure 5. As can be seen in panels (a)–(d), the jump in the magnetic field and speed is greatly reduced with this technique. It is possible to see that some compression in magnetic field persists even after the plasma has been "unshocked." This is due to the decompression method having several limitations. First, the shock parameters are assumed to be fixed throughout the decompression, and they are estimated using a single-spacecraft technique, which is inherently affected by uncertainties (Trotta et al. 2022a). The shock variability, particularly important for supercritical shocks, on a variety of scales (e.g., Marghitu et al. 2017; Kajdič et al. 2019, 2021), may therefore introduce fluctuations in the decompression. Finally, as discussed in the Appendix, the decompression method makes use of the Rankine–Hugoniot jump conditions without including waves and/or turbulence (e.g., Zank et al. 2002; Gedalin 2023). This technique can be further improved, in future studies, to mitigate the above limitations.

The preservation of the SBs' Alfvénicity is evident from Figures 5(a)–(d), where the downstream behavior of the magnetic field and velocity fluctuations is remarkably similar to the upstream one. The analysis of magnetic field excursions further strengthens this point, where compatible behavior between downstream and upstream fluctuations is found. The magnetic field excursion space covered by the downstream fluctuations is still larger, due to some compressive features downstream of the shock not fully removed by the Rankine–Hugoniot decompression. However, we observe that, downstream of the shock, we find larger deflections of the magnetic field. It is also worth noting that, after decompression, the difference in the B_R–B_N plane becomes less evident.

A totally different behavior from that found for SBs is found for the upstream ion cyclotron waves discussed in Section 3.1. The signature of these waves, a clearly visible feature in the reduced magnetic helicity spectrogram (red patches of $\sigma_m = 1$, near the ion plasma frequency, in Figure 3), is completely lost downstream of the shock. We address this interesting feature in Figure 6, where we study how PSP crosses the wave environment surrounding the shock. To this end, we compute the angle between the local magnetic field and the radial direction, $\theta_{\rm BR}$, as well as the angle between the local magnetic field and the local velocity $\theta_{\rm BV}$, where $V = V - V_{\rm PSP}$, where $V_{\rm PSP}$ is the velocity of PSP in the inertial RTN frame. In Figure 6(b), ion cyclotron waves are clearly observed when $\theta_{\rm BV}$ is close to 180° and lost when $\theta_{\rm BV}$ is of the order of 90°. This behavior could be simply due to an observational bias. As shown by Bowen et al. (2020), this phenomenon is the result of measuring a quasi-parallel wavevector at oblique angles, combined with the higher amplitude in the perpendicular direction of the anisotropic turbulent fluctuations. Furthermore, the conditions downstream of the shock inhibit the possibility of resonant beam–field interaction, due to the strongly turbulent environment diffusing the beam in velocity space (e.g., Valentini et al. 2010). We analyzed the ion velocity distribution functions as measured by SPANi, although they were complicated by the limited field of view of the instrument, and we did not find any beam signature downstream of the shock, suggesting that the production mechanisms of ion cyclotron waves are indeed suppressed. A detailed investigation of such features is out of scope for this work and will be the object of further studies.

3.3. The Shock at Solar Orbiter

In this section, we discuss the event as observed by SolO. The shock crossed the spacecraft at 10:00:51 on 2022 September 6. The shock parameters, reported in Table 1, are compatible with the PSP observations. However, as discussed in Section 3.1, shock variability plays a major role in the SolO observations. Here, the shock transition appears far more structured, with an overall behavior compatible with strong shocks.

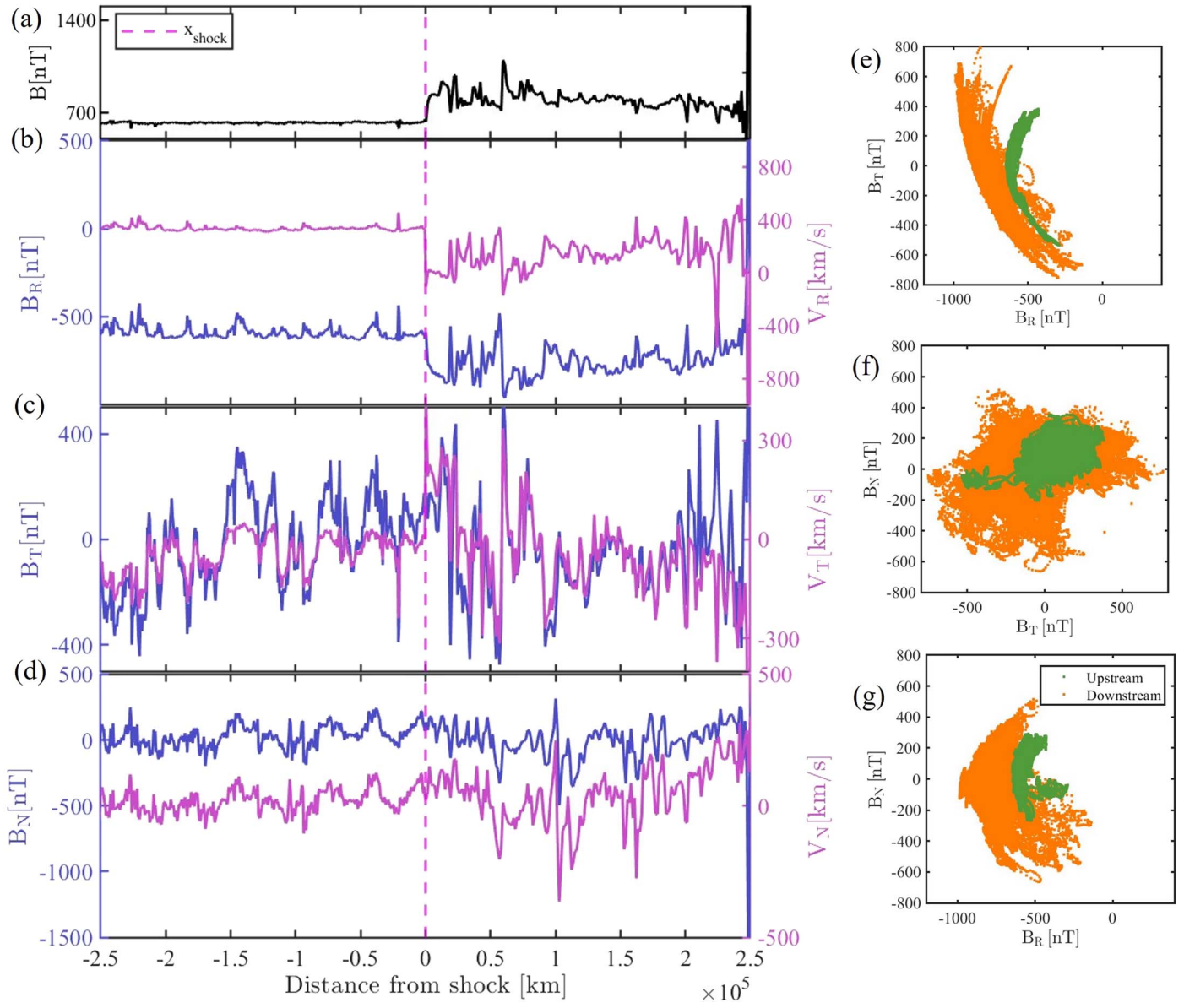

Figure 5. PSP observations of: (a)–(d) magnetic field magnitude (black), magnetic field components (blue), and ion bulk flow speed components (plum), as a function of distance from the shock, where the downstream quantities have been decompressed using the Rankine–Hugoniot relations with the average shock parameters reported in Table 1. (e), (f), and (g) magnetic field excursion scatterplots as in Figure 4, performed on the decompressed quantities. We note that the scales in panels (e), (f), and (g) are different from the ones used in Figure 4.

Such interesting aspects of the SolO shock observations are investigated in Figure 7. The structuring observed in the shock surroundings is particularly evident in the 20 minutes downstream of the shock, populated with many sharp changes of magnetic field (Figure 7). First of all, using the EPD-EPT instrument, we address how the production of energetic particles is affected by such disturbed conditions. As can be seen in Figure 7(a), energetic ions of up to ∼2 MeV are accelerated by the shock, with fluxes rising as the shock crossing is approached, a behavior typical of ion acceleration at IP shocks (Giacalone 2012; Lario et al. 2022). Interestingly, some of the fluxes (e.g., the ones for ∼0.33 and ∼0.7 MeV, shown as green and yellow lines, respectively) have their peaks at times that are not coincident with the shock crossing time at SolO, but instead are downstream of the shock. This behavior, consistent with the statistical study presented in Lario et al. (2003), has implications for the production and propagation of shock-accelerated particles (Perri et al. 2022), and may well be due to additional acceleration mechanisms downstream of the shock (Zank et al. 2015; Zhao et al. 2018; Kilpua et al. 2023).

A crucial feature found for the energetic particle population is the fluctuations found in their fluxes immediately downstream of the shock, with typical timescales of 1–2 minutes, particularly evident for the lower-energy channels (0.05–0.35 MeV, shown in dark blue to green). Such fluctuations correlate well with the magnetic field structuring (Figures 7(a), (b), and (c)), thus suggesting that particle acceleration is indeed happening in an irregular fashion for this IP shock, where additional acceleration may be provided by the magnetic structures (Zhao et al. 2018; Nakanotani et al. 2021; Trotta et al. 2022b). To quantify the variability associated with the shock crossing, the θ_{Bn} and local θ_{BR} angles have been estimated using the local magnetic field, the radial direction, and the average shock normal, as reported in Table 1. It is

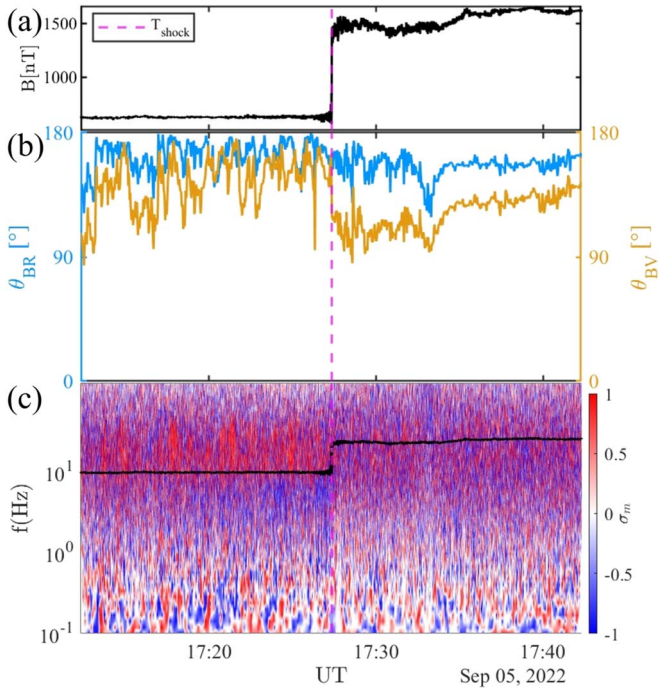

Figure 6. The IP shock interaction with ion cyclotron waves. (a) magnetic field magnitude around the shock crossing by PSP. (b) angle between local magnetic field and radial direction (θ_{BR}, blue) and ion velocity (θ_{BV}, yellow). (c) reduced magnetic helicity for the interval (as in Figure 3).

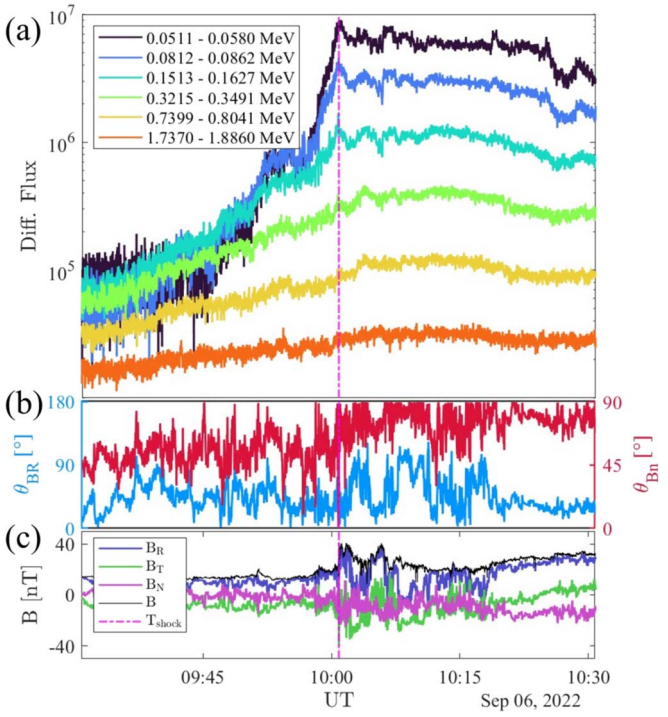

Figure 7. (a) energetic ion fluxes in the ∼0.05–2 MeV energy range as observed by the Sun telescope of the EPD-EPT instrument of Solar Orbiter. (b) local θ_{BR} (blue) and θ_{Bn} (red) angles. (c) magnetic field magnitude (black) and its components. The dashed magenta line indicates the shock crossing time.

evident from this analysis, shown in in Figure 7(b), that the shock geometry changes significantly on the timescales examined here, moving from quasi-perpendicular to quasi-parallel geometries and thus supporting the picture of irregular particle acceleration. Complementing the theme of shock

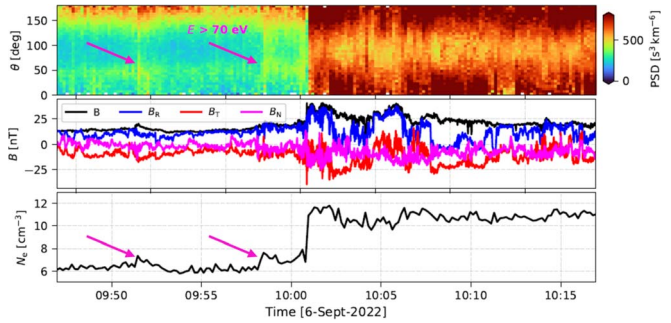

Figure 8. Overview of electron behavior at SolO. Top: EAS electron pitch-angle distributions for particles with energies larger than 70 eV. Middle: magnetic field measurements in RTN. Bottom: electron density computed from EAS measurements.

variability, it is worth discussing the role of plasma structures in particle acceleration. The typical gyroradii of the particles showing such irregular behavior have been estimated using the local magnetic field, $r_L \sim 10^4$ km. Using Taylor's hypothesis, such lengths are comparable to 1/10th of the typical size of the downstream structures, thus suggesting that trapping of accelerated particles may play a role into the variability observed in the particle fluxes, an important source of extra particle acceleration beyond the shock (see Zank et al. 2015; Zhao et al. 2018; Roux et al. 2019; Trotta et al. 2020; Pezzi et al. 2022).

Another extremely interesting feature of the SolO observations is the steep magnetic field enhancements observed in the 10 minutes upstream of the shock (Figure 8). Such steep enhancements are compatible with upstream shocklets, typically arising from the interplay between shock-reflected, energetic ions, and upstream waves—which, in the case of Earth's bow shock, are the Ultra Low Frequency (ULF) waves routinely found in the foreshock (Stasiewicz et al. 2003). Shocklets are important because they influence the plasma environment upstream of the shock transition, thus preconditioning the shock inflow (Lucek et al. 2008). Most of our knowledge of shocklets is built on observations upstream of Earth's bow shock (Plaschke et al. 2018); they are rarely observed at IP shocks, with only three cases previously reported (Lucek & Balogh 1997; Wilson et al. 2009; Trotta et al. 2023a), making this observation particularly interesting.

Two shocklets were observed upstream of the shock at SolO, compatible with the fact that, when estimated at ∼20 minute timescales, the shock Mach number is high and the geometry is quasi-parallel (see discussion in Section 3.1). In Figure 8, using SolO-EAS measurements, we show how the shocklets influence the low-energy electron population, using SolO-EAS measurements. First of all, shocklets are associated with rises in the electron density, identified by the magenta arrows in Figure 8(c), a behavior recently found also at Venus (Collinson et al. 2023). Furthermore, by analyzing the pitch-angle distributions of electrons with energy greater than 70 eV, we found that electrons are more isotropic in pitch-angle space in the vicinity of the shocklets, probably due to pitch-angle scattering induced by the compressive structures, as observed in the Earth's bow shock environment (Wilson et al. 2013). This behavior, namely the preconditioning of the upstream particle population, may have important consequences for electron injection and acceleration to higher energies (Katou & Amano 2019; Dresing et al. 2022; Wijsen et al. 2023).

4. Conclusions

The 2022 September 5 CME event provided an opportunity to study a CME-driven IP shock at unprecedentedly low heliocentric distance, with PSP crossing the event at 0.07 au. Furthermore, the radially well-aligned SolO at 0.7 au provided important insights about the evolution of the event.

We focused on the small-scale behavior of CME-driven shocks associated with this event. The PSP spacecraft observed the shock very early in its evolution. The shock had moderate Mach numbers ($M_A \sim M_{\rm fms} \sim 4$)), as inferred using local shock parameter estimation. The average shock normal was found to be $\hat{n} = (0.5, -0.8, 0.2)$, significantly departing from the radial direction, indicating that the crossing of the shock likely happened on one flank of the CME event. This has also important implications when addressing the joint PSP–SolO observations, as the shock will be crossed in different locations, with features depending on the CME width and spacecraft longitudinal separation. The shock at PSP has a notably short sheath region, due to its early evolutionary stage, an interesting property that may have fundamental implications for the possibility of accelerating particles to high energies, as preliminarily shown in Cohen et al. (2023). However, we emphasize that, as this event was crossed at the flanks of the sheath, the CME flux-rope boundary cannot be determined accurately.

We studied how switchbacks, fundamental constituents of the solar wind, as elucidated by several previous PSP observations (e.g., Bale et al. 2019; Kasper et al. 2019; Dudok de Wit et al. 2020), are processed in the shock crossing. We found that the SBs are compressed along the shock-normal direction and stretched along the other two directions. Interestingly, many SBs properties are preserved in the shock downstream. Furthermore, SBs with larger magnetic field deflections were found in the shock downstream, an important factor to consider when addressing their statistical properties. Such statistical properties of how SBs are processed by IP shocks will be object of future investigation, now increasingly possible thanks to the novel PSP ShOck Detection Algorithm (SODA) IP shock list.[19] This behavior has been investigated in detail by looking at the decompressed magnetic field and plasma quantities, obtained using the Rankine–Hugoniot shock jump conditions. This technique of decompression is useful to estimate the values of quantities before their interaction with the shock. It can also be used to yield an estimate of how the ambient plasma conditions could change due to the passage of a shock with a given set of parameters, as will be shown in future work.

How ion cyclotron waves are transmitted across the shock was also addressed. This study is particularly interesting due to the role that ion cyclotron waves play in energy dissipation (e.g., Bowen et al. 2022). We observe that the signature of preexisting ion cyclotron waves, identified in the shock upstream at PSP, disappears downstream of the shock (Figure 6). This may be due to the sudden change in plasma conditions at the shock, injecting strong fluctuations in the downstream, making the conditions for ion cyclotron waves propagation less favorable. Through the analysis of the $\theta_{\rm BV}$ and $\theta_{\rm BR}$ angles, we also found unfavorable conditions for detecting ion cyclotron activity downstream (Bowen et al. 2020), due to the change of the mean magnetic field direction upon the shock passage.

SolO observations of the same event are extremely interesting with regard to addressing the role of evolution of the CME shock region in its propagation to larger heliocentric distances. On large scales, we note that the large transverse flow deflections are still present, with a V_N increase comparable to the one observed in V_R.

The shock environment at SolO is much more disturbed than the one observed at PSP. A shock parameter estimation using very short averaging windows (∼1 minute, thus addressing the very local shock properties) yields similar values with respect to the PSP observations (see Table 1). However, analyzing the 30 minutes across the shock transition, we find an environment compatible with a quasi-parallel shock and relatively high Mach number, propagating in a very structured portion of the solar wind. Two shocklets, structures that grow favorably upstream of high Mach number, quasi-parallel shocks, were found upstream of the shock, a rare observation for the interplanetary case. Signatures of ∼100 eV electron scattering were found corresponding to the shocklets, an important factor to be considered in the preconditioning of the upstream particle population at the shock. It is worth noting that these shocklets, with durations much larger than those observed at Earth's bow shock, probably arise from pre-existing upstream waves and not from shock-generated upstream waves, a behavior observed also for the case in Trotta et al. (2023a). Therefore, this observation points to the idea that the origin of the IP shocklets is different from those observed in the Earth's foreshock.

Energetic ions up to 2 MeV were found in association with the shock at SolO. A detailed analysis of the high time resolution EPD-EPT energetic particle fluxes reveals structuring corresponding to the magnetic field structures processed by the shock, indicating the potential role of trapping as an extra source of energy for particle acceleration.

Finally, we underline that this event is a very good example of the novel observational window provided by missions exploring the inner heliosphere such as PSP and SolO, exploited in this study to highlight the fact that the features of IP shock environments can be very different as they propagate through the heliosphere, with important consequences for the accuracy of the modeling effort and the possibility of predictions associated with such energetic events.

Acknowledgments

This work has received funding from the European Union's Horizon 2020 research and innovation program under grant agreement No. 101004159 (SERPENTINE, www.serpentine-h2020.eu). A.L. is supported by STFC Consolidated grant ST/T00018X/1. C.H.K.C. is supported by UKRI Future Leaders Fellowship MR/W007657/1 and STFC Consolidated Grants ST/T00018X/1 and ST/X000974/1. H.H. is supported by the Royal Society University Research Fellowship URF/R1/180671. N.D. is grateful for support by the Academy of Finland (SHOCKSEE, grant No. 346902). The PSP/FIELDS experiment was developed and is operated under NASA contract NNN06AA01C. Work at IRAP is supported by CNRS, UPS, and CNES. E.E.D acknowledges funding by the European Union (ERC, HELIO4CAST, 101042188). Views and opinions expressed are, however, those of the author(s) only and do not necessarily reflect those of the European Union or the European Research Council Executive Agency. Neither

[19] https://parker.gsfc.nasa.gov/shocks.html

the European Union nor the granting authority can be held responsible for them. X.B.C. is grateful for PAPIIT DGAPA grant IN110921. This work was supported by the UK Science and Technology Facilities Council (STFC) grant ST/W001071/1. L.F. is supported by the Royal Society University Research Fellowship No. URF\R1\231710. R.F.W.S. thanks the German Space Agency (DLR) for its support of SOLO/EPD under grant 50OT2002.

Appendix
Rankine–Hugoniot Decompression Method

Heliospheric shocks crossing spacecraft can be directly measured. An hypothesis that is often made when interpreting spacecraft measurements is the Taylor hypothesis (Taylor 1938), linking time variations in the spacecraft measured quantities to spatial variations. Thus, upon shock crossing, it is possible to address the properties of the upstream/downstream shock environments (see Figure 2). However, it is often the case that it would be interesting to address the shock downstream plasma *before it was shocked*, as discussed in Section 3.2. Here, we present a technique providing a proxy to address the condition of the plasma prior to the shock propagation.

The Rankine–Hugoniot jump conditions (e.g., Burgess & Scholer 2015) have been widely used to model the plasma properties across a shock. Here, the shock is treated as a planar, one-dimensional, time-stationary structure. Following an integration of the MHD equations for mass, momentum, and energy conservation, and the divergence-free condition for the magnetic field, the Rankine–Hugoniot relations linking the properties of upstream and downstream plasmas can be written as follows:

$$\frac{\rho_{m2}}{\rho_{m1}} = r_{\rm gas} \tag{A1}$$

$$\frac{V_{n2}}{V_{n1}} = \frac{1}{r_{\rm gas}} \tag{A2}$$

$$\frac{V_{t2}}{V_{t1}} = \frac{M_{A1}^2 - 1}{M_{A1}^2 - r_{\rm gas}} \tag{A3}$$

$$\frac{B_{n2}}{B_{n1}} = 1 \tag{A4}$$

$$\frac{B_{t2}}{B_{t1}} = r_{\rm gas}\frac{M_{A1}^2 - 1}{M_{A1}^2 - r_{\rm gas}} \tag{A5}$$

$$\frac{P_2}{P_1} = r_{\rm gas} + \frac{(\gamma - 1) r_{\rm gas} V_1^2}{2 V_S 1}\left(1 - \frac{V_2^2}{V_1^2}\right). \tag{A6}$$

The above equations for density, bulk flow velocity, magnetic field, and pressure (ρ_m, V, B, and P, respectively) are expressed in the de Hoffmann–Teller frame, i.e., a frame aligned to the shock normal that moves at a speed such that the upstream convective electric field ($E_1 = -V_1 \times B_1$) vanishes (de Hoffmann & Teller 1950). Here, the subscripts 1 and 2 are referred to as the upstream and downstream states, respectively. The subscripts n and t instead indicate the shock-normal and tangential directions. $r_{\rm gas}$ is the shock gas compression ratio, and $M_{A1} \equiv V_{n1}\sqrt{\mu_0 \rho_{m1}}/B_{n1}$ is the Alfvénic Mach number. V_{S1} is the upstream sound speed.

Often, the Rankine–Hugoniot equations are used to address shock parameters. What we do in our decompression technique is instead to use the downstream measurements and the shock parameters to compute the upstream conditions, thus "unshocking" the plasma according to Equations (A1)–(A6). The procedure, given a time series of spacecraft measurements, is performed as follows (and displayed in Figure 9). First, the data are rotated in a shock-normal frame. Here, we choose the *nlm* frame, where the n direction is aligned with the shock normal (computed using the MX3 method (Paschmann & Schwartz 2000)), m is perpendicular both to the shock normal and to the upstream magnetic field, and l completes the triad. We then perform a velocity transformation to the deHoffman–Teller frame of the shock. Then, Equations (A1)–(A6) are used to derive the upstream quantities, given the downstream measurements and the shock parameters, i.e., the decompression is performed. The data are then returned in the spacecraft frame. Finally, using the mean upstream and downstream flow speeds, it is possible to show the measurements in units of distance from shock (see Figure 5).

This technique, while giving a proxy for the plasma conditions before shock processing, has several limitations. The decompression is performed assuming that the shock parameters do not change throughout the event, thus neglecting the inherent variability of shock system. Shock parameters are estimated from single spacecraft measurements, and therefore they are associated with uncertainties. The Rankine–Hugoniot relations used to decompress the plasma assume a one-dimensional, planar, time-stationary MHD shock with laminar upstream/downstream regions, which is notoriously a stringent assumption for heliosphere shocks, which are characterized by several space/time variabilities and propagate in the turbulent solar wind.

For the above reasons, it is readily understood that the decompression is more reliable for closer measurements with respect to the shock crossing. In Figure 9, it is possible to see how unphysical results are introduced by the large structure embedded in the plasma happening around 17:33 UT. Future improvements of the diagnostic—for example, including wave transmission—will be the objective of future work.

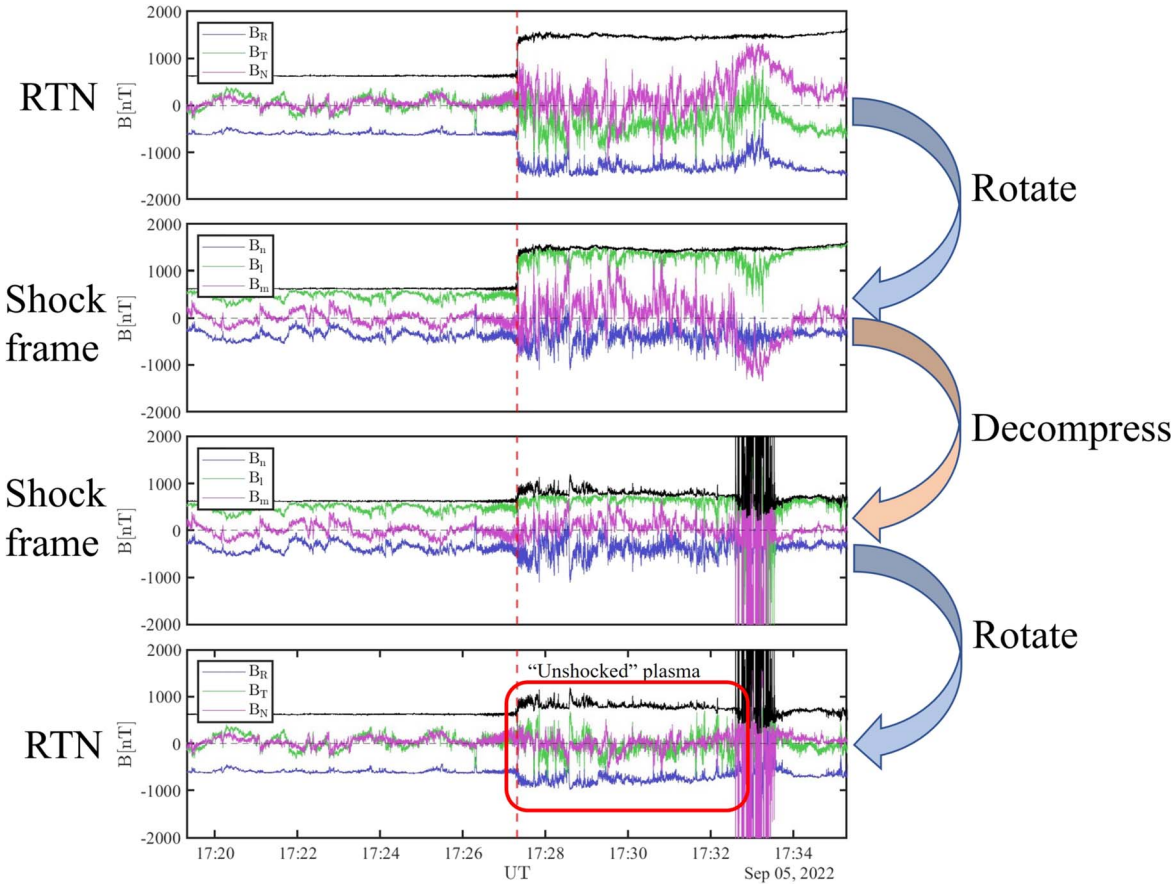

Figure 9. Overview of the procedure of magnetic field decompression.

ORCID iDs

Domenico Trotta https://orcid.org/0000-0002-0608-8897
Andrea Larosa https://orcid.org/0000-0002-7653-9147
Georgios Nicolaou https://orcid.org/0000-0003-3623-4928
Timothy S. Horbury https://orcid.org/0000-0002-7572-4690
Lorenzo Matteini https://orcid.org/0000-0002-6276-7771
Heli Hietala https://orcid.org/0000-0002-3039-1255
Xochitl Blanco-Cano https://orcid.org/0000-0001-7171-0673
Luca Franci https://orcid.org/0000-0002-7419-0527
C. H. K Chen https://orcid.org/0000-0003-4529-3620
Lingling Zhao https://orcid.org/0000-0002-4299-0490
Gary P. Zank https://orcid.org/0000-0002-4642-6192
Christina M. S. Cohen https://orcid.org/0000-0002-0978-8127
Stuart D. Bale https://orcid.org/0000-0002-1989-3596
Ronan Laker https://orcid.org/0000-0002-6577-5515
Nais Fargette https://orcid.org/0000-0001-6308-1715
Francesco Valentini https://orcid.org/0000-0002-1296-1971
Yuri Khotyaintsev https://orcid.org/0000-0001-5550-3113
Rungployphan Kieokaew https://orcid.org/0000-0003-0937-2655
Nour Raouafi https://orcid.org/0000-0003-2409-3742
Emma Davies https://orcid.org/0000-0001-9992-8471
Rami Vainio https://orcid.org/0000-0002-3298-2067
Nina Dresing https://orcid.org/0000-0003-3903-4649
Emilia Kilpua https://orcid.org/0000-0002-4489-8073
Tomas Karlsson https://orcid.org/0000-0002-4546-5050
Christopher J. Owen https://orcid.org/0000-0002-5982-4667
Robert F. Wimmer-Schweingruber https://orcid.org/0000-0002-7388-173X

References

Adhikari, L., Zank, G. P., Telloni, D., & Zhao, L.-L. 2022, ApJL, 937, L29
Bale, S. D., Badman, S. T., Bonnell, J. W., et al. 2019, Natur, 576, 237
Bale, S. D., Drake, J. F., McManus, M. D., et al. 2023, Natur, 618, 252
Bale, S. D., Goetz, K., Harvey, P. R., et al. 2016, SSRv, 204, 49
Barnes, A., & Hollweg, J. V. 1974, JGR, 79, 2302
Blanco-Cano, X., Burgess, D., Sundberg, T., & Kajdič, P. 2019, JGRA, 124, 9760
Blanco-Cano, X., Kajdič, P., Aguilar-Rodríguez, E., et al. 2016, JGRA, 121, 992
Bowen, T. A., Chandran, B. D. G., Squire, J., et al. 2022, PhRvL, 129, 165101
Bowen, T. A., Mallet, A., Huang, J., et al. 2020, ApJS, 246, 66
Burgess, D., & Scholer, M. 2015, Collisionless Shocks in Space Plasmas (Cambridge: Cambridge Univ. Press)
Burton, M. E., Smith, E. J., Goldstein, B. E., et al. 1992, GeoRL, 19, 1287
Bykov, A. M., Vazza, F., Kropotina, J. A., Levenfish, K. P., & Paerels, F. B. S. 2019, SSRv, 215, 14
Cohen, C., Christian, E., Cummings, A. C., et al. 2023, ICRC (Nagoya), 38, 1276
Collinson, G. A., Hietala, H., Plaschke, F., et al. 2023, GeoRL, 50, e2023GL104610
de Hoffmann, F., & Teller, E. 1950, PhRv, 80, 692
Dessler, A. J., & Fejer, J. A. 1963, P&SS, 11, 505
Dresing, N., Kouloumvakos, A., Vainio, R., & Rouillard, A. 2022, ApJL, 925, L21
Dresing, R. L., Jebaraj, I. C., et al. 2023, A&A, 674, A105
Dudok de Wit, T., Krasnoselskikh, V. V., Bale, S. D., et al. 2020, ApJS, 246, 39
Dungey, J. W. 1979, NCimC, 2C, 655
Eastwood, J. P., Hietala, H., Toth, G., et al. 2015, SSRv, 188, 251
Farrell, W. M., MacDowall, R. J., Gruesbeck, J. R., Bale, S. D., & Kasper, J. C. 2020, ApJS, 249, 28
Fox, N. J., Velli, M. C., Bale, S. D., et al. 2016, SSRv, 204, 7
Gedalin, M. 2023, ApJ, 958, 2
Giacalone, J. 2005, ApJL, 628, L37
Giacalone, J. 2012, ApJ, 761, 28

Giacalone, J., Burgess, D., Bale, S. D., et al. 2021, ApJ, 921, 102
Gieseler, J., Dresing, N., Palmroos, C., et al. 2023, FrASS, 9, 384
Gosling, J. T., Hildner, E., MacQueen, R. M., et al. 1974, JGR, 79, 4581
Gosling, J. T., McComas, D. J., Roberts, D. A., & Skoug, R. M. 2009, ApJL, 695, L213
Guo, F., Giacalone, J., & Zhao, L. 2021, FrASS, 8, 27
Horbury, T. S., O'Brien, H., Carrasco Blazquez, I., et al. 2020, A&A, 642, A9
Jagarlamudi, V. K., Raouafi, N. E., Bourouaine, S., et al. 2023, ApJL, 950, L7
Kajdič, P., Pfau-Kempf, Y., Turc, L., et al. 2021, JGRA, 126, e2021JA029283
Kajdič, P., Preisser, L., Blanco-Cano, X., Burgess, D., & Trotta, D. 2019, ApJL, 874, L13
Kasper, J. C., Abiad, R., Austin, G., et al. 2016, SSRv, 204, 131
Kasper, J. C., Bale, S. D., Belcher, J. W., et al. 2019, Natur, 576, 228
Katou, T., & Amano, T. 2019, ApJ, 874, 119
Khotyaintsev, G. D. B., Vaivads, A., et al. 2021, A&A, 656, A19
Kilpua, E., Koskinen, H. E. J., & Pulkkinen, T. I. 2017, LRSP, 14, 5
Kilpua, E., Vainio, R., Cohen, C., et al. 2023, Ap&SS, 368, 66
Kilpua, E. K., Lumme, E., Andreeova, K., Isavnin, A., & Koskinen, H. E. 2015, JGRA, 120, 4112
Krasnoselskikh, V., Larosa, A., Agapitov, O., et al. 2020, ApJ, 893, 93
Krehl, P. O. K. 2015, EPJH, 40, 204
Kropotina, J. A., Webster, L., Artemyev, A. V., et al. 2021, ApJ, 913, 142
Lai, H. R., Russell, C. T., Jian, L. K., et al. 2012, SoPh, 278, 421
Lario, D., Ho, G. C., Decker, R. B., et al. 2003, in AIP Conf. Proc. 679, Solar Wind Ten, ed. M. Velli (Melville, NY: AIP), 640
Lario, D., Richardson, I. G., Wilson, L. B. I., et al. 2022, ApJ, 925, 198
Larosa, A., Krasnoselskikh, V., Dudok de Wit, T., et al. 2021, A&A, 650, A3
Liang, H., Zank, G. P., Nakanotani, M., & Zhao, L.-L. 2021, ApJ, 917, 110
Liu, Y. D., Ran, H., Hu, H., & Bale, S. D. 2023, ApJ, 944, 116
Livi, R., Larson, D. E., Kasper, J. C., et al. 2022, ApJ, 938, 138
Long, D. M., Green, L. M., Pecora, F., et al. 2023, ApJ, 955, 152
Lucek, E. A., & Balogh, A. 1997, GeoRL, 24, 2387
Lucek, E. A., Horbury, T. S., Dandouras, I., & Rème, H. 2008, JGRA, 113, A07S02
Maksimovic, M., Bale, S. D., Chust, T., et al. 2020, A&A, 642, A12
Marghitu, O., Comişel, H., & Scholer, M. 2017, GeoRL, 44, 6500
Matteini, L., Horbury, T. S., Pantellini, F., Velli, M., & Schwartz, S. J. 2015, ApJ, 802, 11
Matthaeus, W. H., Goldstein, M. L., & Smith, C. 1982, PhRvL, 48, 1256
McComas, D. J., Sharma, T., Christian, E. R., et al. 2023, ApJ, 943, 71
Moncuquet, M., Meyer-Vernet, N., Issautier, K., et al. 2020, ApJS, 246, 44
Müller, D., St. Cyr, O. C., Zouganelis, I., et al. 2020, A&A, 642, A1
Nakanotani, M., Zank, G. P., & Zhao, L.-L. 2021, ApJ, 922, 219
Nakanotani, M., Zank, G. P., & Zhao, L.-L. 2022, ApJ, 926, 109
Nicolaou, W. R. T., Owen, C. J., et al. 2021, A&A, 656, A10
Owen, C. J., Bruno, R., Livi, S., et al. 2020, A&A, 642, A16
Park, B., Pitňa, A., Šafránková, J., et al. 2023, ApJL, 954, L51
Paschmann, G., & Schwartz, S. J. 2000, ESA Special Publication, Vol. 449, Cluster-II Workshop: Multiscale/Multipoint Plasma Measurements (Noordwijk: ESA), 99
Pecora, F., Matthaeus, W. H., Primavera, L., et al. 2022, ApJL, 929, L10
Pérez-Alanis, C. A., Janvier, M., Nieves-Chinchilla, T., et al. 2023, SoPh, 298, 60
Perri, S., Bykov, A., Fahr, H., Fichtner, H., & Giacalone, J. 2022, SSRv, 218, 26
Pezzi, O., Blasi, P., & Matthaeus, W. H. 2022, ApJ, 928, 25
Pitna, A., Zank, G. P., Nakanotani, M., et al. 2023, in Journal of Physics: Conf. Ser. 2544 (Journal of Physics Conference Series), 012009
Pitňa, A., Šafránková, J., Němeček, Z., & Franci, L. 2017, ApJ, 844, 51
Pitňa, A., Šafránková, J., Němeček, Z., Ďurovcová, T., & Kis, A. 2021, FrP, 8, 654
Plaschke, F., Hietala, H., Archer, M., et al. 2018, SSRv, 214, 81
Raouafi, N. E., Matteini, L., Squire, J., et al. 2023, SSRv, 219, 8
Reames, D. V. 1999, SSRv, 90, 413
Richardson, I. G. 2018, LRSP, 15, 1
Richardson, J. D. 2011, JASTP, 73, 1385
Rodríguez-Pacheco, J., Wimmer-Schweingruber, R. F., Mason, G. M., et al. 2020, A&A, 642, A7
Romeo, O. M., Braga, C. R., Badman, S. T., et al. 2023, ApJ, 954, 168
Roux, J. A. L., Webb, G. M., Khabarova, O. V., Zhao, L.-L., & Adhikari, L. 2019, ApJ, 887, 77
Sahraoui, F., Hadid, L., & Huang, S. 2020, RvMPP, 4, 4
Schwartz, S. J., Goodrich, K. A., Wilson, L. B., III, et al. 2022, JGRA, 127, e2022JA030637
Stasiewicz, K., Longmore, M., Buchert, S., et al. 2003, GeoRL, 30, 2241
Sundberg, T., Haynes, C. T., Burgess, D., & Mazelle, C. X. 2016, ApJ, 820, 21
Taylor, G. I. 1938, RSPSA, 164, 476
Telloni, D., Carbone, F., Bruno, R., et al. 2019, ApJL, 885, L5
Trotta, D., Franci, L., Burgess, D., & Hellinger, P. 2020, ApJ, 894, 136
Trotta, D., Hietala, H., Horbury, T., et al. 2023a, MNRAS, 520, 437
Trotta, D., Pecora, F., Settino, A., et al. 2022b, ApJ, 933, 167
Trotta, D., Pezzi, O., Burgess, D., et al. 2023b, MNRAS, 525, 1856
Trotta, D., Valentini, F., Burgess, D., & Servidio, S. 2021, PNAS, 118, e2026764118
Trotta, D., Vuorinen, L., Hietala, H., et al. 2022a, FrASS, 9, 1005672
Turc, L., Roberts, O. W., Verscharen, D., et al. 2023, NatPh, 19, 78
Valentini, F., Iazzolino, A., & Veltri, P. 2010, PhPl, 17, 052104
Verniero, J. L., Larson, D. E., Livi, R., et al. 2020, ApJS, 248, 5
Webb, D. F., & Howard, T. A. 2012, LRSP, 9, 3
Wijsen, N., Lario, D., Sánchez-Cano, B., et al. 2023, ApJ, 950, 172
Wilkinson, W. P. 2003, P&SS, 51, 629
Wilson, L. B. I., Cattell, C. A., Kellogg, P. J., et al. 2009, JGRA, 114, A10106
Wilson, L. B., III, Koval, A., Sibeck, D. G., et al. 2013, JGRA, 118, 957
Woodham, L. D., Wicks, R. T., Verscharen, D., & Owen, C. J. 2018, ApJ, 856, 49
Yang, L., Heidrich-Meisner, V., Berger, L., et al. 2023, A&A, 673, A73
Zank, G. P., Hunana, P., Mostafavi, P., et al. 2015, ApJ, 814, 137
Zank, G. P., Nakanotani, M., Zhao, L.-L., Adhikari, L., & Telloni, D. 2020, ApJ, 900, 115
Zank, G. P., Nakanotani, M., Zhao, L. L., et al. 2021, ApJ, 913, 127
Zank, G. P., Zhou, Y., Matthaeus, W. H., & Rice, W. K. M. 2002, PhFl, 14, 3766
Zhao, L.-L., Zank, G. P., Khabarova, O., et al. 2018, ApJL, 864, L34
Zhao, Z. G. P., He, J. S., et al. 2021, A&A, 656, A3